

Atomic resolution analysis of extended defects and Mg agglomeration in Mg-ion-implanted GaN and their impacts on acceptor formation

Emi Kano¹, Keita Kataoka², Jun Uzuhashi³, Kenta Chokawa¹, Hideki Sakurai^{1,4†}, Akira Uedono⁵, Tetsuo Narita², Kacper Sierakowski⁶, Michal Bockowski^{1,6}, Ritsuo Otsuki⁷, Koki Kobayashi⁷, Yuta Itoh⁷, Masahiro Nagao¹, Tadakatsu Ohkubo³, Kazuhiro Hono³, Jun Suda^{1,7}, Tetsu Kachi¹, and Nobuyuki Ikarashi¹

1. *Institute of Materials and Systems for Sustainability, Nagoya University, Aichi 464-8601, Japan*
2. *Toyota Central R&D Labs., Inc., Nagakute, Aichi 480-1192, Japan*
3. *National Institute for Materials Science, Tsukuba 305-0047, Japan*
4. *Institute of Advanced Technology, ULVAC, Inc., Chigasaki, Kanagawa 253-8543, Japan*
5. *Division of Applied Physics, Faculty of Pure and Applied Science, University of Tsukuba, Tsukuba, Ibaraki 305-8573, Japan*
6. *Institute of High Pressure Physics Polish Academy of Sciences, Sokolowska 29/37, 01-142 Warsaw, Poland*
7. *Department of Electronics, Graduate School of Engineering, Nagoya University, Aichi 464-8603, Japan*

[†]Present affiliation: *ADDC, Toshiba Electronic Devices & Storage Corporation, Ishikawa 923-1293*

Abstract

We carried out atomic-scale observations of Mg-ion-implanted GaN by transmission electron microscopy (TEM) and atom probe tomography (APT) to clarify the crystallographic structures of extended defects and Mg agglomerations that form during post-implantation annealing. The complementary TEM and APT analyses have shown that Mg atoms agglomerate at dislocations that bound extended defects. The concentration of Mg is higher at the dislocations with a larger Burgers vector. This indicates that the Mg agglomeration is caused by the pressure at the dislocations. The Mg concentration in the highly Mg-rich regions is 1 atomic %, which exceeds the solubility limit of Mg in GaN. We investigated isothermal and isochronal evolution of the defects by TEM, cathodoluminescence analysis and positron annihilation spectroscopy. The results indicated that the intensity of donor-acceptor-pair emission increases with the annealing temperature and duration, and reaches a maximum after elimination of the extended defects with highly Mg-rich regions. These results strongly suggest that such extended defects reduce the acceptor formation and that they, as well as the previously reported compensating centers such as N-related vacancies, can inhibit the formation of *p*-type GaN. The mechanism by which the extended defects reduce acceptor formation is discussed.

I. Introduction

Gallium nitride (GaN)-based power devices have been developed to open up new application fields of semiconductor power devices: Since GaN has a breakdown electric field higher than that of other semiconducting materials in practical use,^{1,2} GaN-based power device technology can realize higher power and higher efficiency devices. To unleash the full potential of GaN devices for high voltage applications, selective area doping using ion implantation is indispensable.³⁻⁸ However, ion-implanted magnesium (Mg) atoms exhibit an activation ratio lower than that of Mg atoms doped in epitaxially grown GaN.^{7,9-12} Mg is the dopant most commonly used to generate *p*-type conductivity in GaN. Recently, we have shown that Mg ion-implanted GaN exhibits *p*-type conductivity after annealing at temperatures of 1673 K and higher.^{8,11,13}

We have examined crystallographic structures of extended defects formed after post-implantation annealing by transmission electron microscopy (TEM).^{14,15} Defects visible in TEM, as distinguished from invisible ones, such as the point defects and their complexes, are referred to hereafter as extended defects. We found nano-scale intrinsic defects and intrinsic dislocation loops lying on $\{11\bar{2}0\}$ in the samples in which the Mg acceptors were fully activated after high temperature or prolonged annealing.^{14,15} In contrast, nano-scale extrinsic stacking faults and defects with inversion domains (IDs) were found in the samples in which the Mg acceptors were not fully activated.^{14,15} We also showed that Mg atoms at the (0001) ID boundaries (IDBs) are electrically inactive, *i.e.*, they do not act as acceptors. Atom probe tomography (APT) showed local increase in Mg concentration occurred in the samples annealing at and above 1373 K.¹⁶ These results indicate that such local increase in Mg concentration does not have random nature and that Mg atoms might agglomerate at some crystallographic defects.¹⁶ However, the crystallographic structures of the defects at which the Mg atoms agglomerate have yet to be clarified.^{14,16} The cause of the Mg agglomeration and the impacts of the agglomerations on acceptor formation have not been fully understood.^{16,17} In this study, we have revealed the atomic structures of the defects for better understanding of the cause of the Mg agglomeration and the impact of the defects and the agglomerations on the Mg acceptor formation.

Cathodoluminescence spectroscopy (CL) has been used to investigate the acceptor formation and its compensation via point defects.^{8,9,18-21} Positron annihilation spectroscopy (PAS) has been employed in characterizing vacancy-type point defects and their complexes and in measuring their concentrations.^{22,23} CL and PAS measurements have shown how the annealing temperature and duration affect the acceptor formation and the concentrations of the point defects and their complexes.^{8,9,22,23} Since extended defects grow or shrink by capture or emission of point defects, isochronal and isothermal analysis of the extended defects using TEM and APT in combination with CL and PAS should provide a further understanding of the evolution of the extended defects as well as the relation between their correlation with the acceptor activation.

The purpose of this study is to clarify the impact of the extended defects and the Mg

agglomerations on the acceptor formation in Mg-ion-implanted GaN. We first examine extended defects that form during post-implantation annealing and clarify their crystallographic features, such as their Burgers vectors using TEM. We also examine the relationship between the extended defects and Mg agglomeration using TEM and APT. We then investigate the relation between the extended defects and the acceptor formation through isochronal and isothermal analyses of the evolution of extended defects using TEM, CL and PAS. The impact of the evolution of the extended defects on the Mg acceptor formation is discussed.

II. Experimental methods

Undoped GaN epitaxial layers were grown by metalorganic vapor phase epitaxy on free-standing GaN (0001) substrates. Mg ions were implanted at room temperature to generate a box-shaped Mg profile to a depth of 300 nm. The Mg concentration measured by secondary ion mass spectrometry (SIMS) was $1 \times 10^{19} \text{ cm}^{-3}$. Table I shows the temperatures and the durations of the annealing for the samples examined in the present experiments. The isochronal annealing was carried out at 1573 K, 1673 K and 1753 K for 5 min (C1 to C3). The isothermal annealing was carried out at 1573 K for 0.5 min to 120 min (T0 to T5). In the annealing of sample T0, the temperature of the sample was dropped just after it reached 1573K. All the annealing runs were performed under a N_2 partial pressure of 1 GPa.⁸ The temperature was raised at a rate of 26.7 K/min.

We examined the structures of extended defects using scanning TEM (STEM) of a JEOL ARM-200F. The acceleration voltage was 200 kV and the spherical aberration coefficient was smaller than 1 μm . In high-angle annular dark-field (HAADF) STEM observations, the inner and outer angles of the annular dark-field (ADF) detector were 50 and 150 mrad, respectively. Energy dispersive x-ray spectroscopy (EDS) was used to detect Mg agglomerated at defects in the samples. The specimens for TEM were prepared by mechanical thinning followed by Ar-ion milling. A low-energy Ar-ion beam (1 keV) and a liquid-nitrogen-cooled stage were used to reduce artifacts produced by ion milling. APT analyses to obtain three-dimensional Mg distributions were conducted by using a CAMECA LEAP 5000XS. APT specimens were prepared by the FEI Helios G4UX, a focused ion beam instrument with a scanning electron microscopy system, using a standard lift-out method. APT measurements were carried out with 250 kHz 355 nm UV laser pulsing at a specimen temperature of 30 K. The laser pulse energy was set to 10 fJ. In this measurement condition, the detection limit of Mg by APT is 10^{17} to 10^{18} cm^{-3} .²⁴ The APT data were visualized by CAMECA Integrated Visualization and Analysis Software (IVAS) 3.8 and AP Suite Software.

CL analyses were carried out at a sample temperature of 10 K. The acceleration voltage and probe current density were 5 keV and $8.3 \times 10^{-5} \text{ A/cm}^2$. Intensity of donor-acceptor pair (DAP) luminescence around 3.28 eV indicates Mg acceptor formation.^{18,19} Broad green luminescence (GL) around 2.35 eV is commonly observed in Mg ion-implanted GaN and has been assigned to a transition

involving nitrogen vacancy (V_N) related defects.^{9,20,21} V_N -related defects reportedly act as compensating centers in *p*-type GaN.²⁵ In the PAS analysis, the line-shape parameter S of the Doppler broadened profile was used to detect vacancy-type defects in the samples.²⁶ The S parameter represents the sizes and concentrations of vacancy-type defects. S parameters measured at the incident energy of positrons E in the range between 4 and 7 keV were averaged to increase the statistical accuracy. The mean implantation depth of positrons in this energy range is about 80 nm. Measurements were carried out in darkness and with illumination with a He–Cd laser.²⁷ The value of S can be changed by illuminating samples with a He–Cd laser (wavelength of 325 nm), and this change is attributed to the capture of photon-excited electrons by the vacancy defects. The capture of the electrons change the charge state of the defects from positive to neutral (V_+ to V_0) or from neutral to negative (V_0 to V_-) and can increase the probability of positrons being trapped at defects.²⁷ Hence, the measurement with the laser illumination enables detection of donor-like vacancies.²⁸

III. Results

A. TEM and APT results

Figure 1 shows the evolution of extended defects during the isochronal annealing (Figs. 1(a)-(c): samples C1-C3) and the isothermal annealing (Figs. 1(a), (d)-(f): samples C1, T1, T2, and T5). Micrographs are ADF-STEM cross-sectional images of the samples viewed in the $[11\bar{2}0]$ direction. Four types of extended defects are observed. That is, bright oblongs and dots are seen in samples C1 and T1, and indicate type α and β defects, respectively. Bright loops and dots are seen in samples C2, C3, T2, and T5, and indicate type γ and δ defects, respectively.

The TEM images of samples C1, C2, and C3 show that α and β defects form during lower-temperature annealing (sample C1), and γ and δ defects form during higher-temperature annealing (samples C2 and C3). TEM images of samples C1 and T1 to T5 show that α and β defects form during shorter-duration-annealing (samples C1 and T1), and γ and δ defects form during longer-duration-annealing (samples T2 and T5). Figures 1(a) and 1(d) indicate that the oblong-shaped α defect changes into a circular-shaped defect as it becomes larger (from C1 to T1). This suggests that the defect changes its shape to reduce the length of the perimeter of its defect area and to increase the curvature radius of the dislocation segments because reducing the length of the perimeter and increasing the curvature radius reduces the total dislocation energy of the defect.²⁹ The α and β defects were mainly found in the depth region 200 to 500 nm from the sample surface. The evolution of the defects seen in the present analyses is consistent with previous observations.¹⁴ Therefore the same defect evolution was observed in the isochronal and the isothermal annealing: α and β defects were observed in the early stage of the annealing (samples C1 and T1), and γ and δ defects were found in the later stages (samples C2, C3, and T2-T5).

We examined the structural details of the extended defects to clarify their crystallographic

features, such as their Burgers vectors. TEM results for an α defect are shown in Fig. 2. Fig. 2(a) shows a HAADF-STEM image of the defect. The incident beam direction is $\langle 1\bar{1}00 \rangle$, which is orthogonal to that used in Fig. 1, $\langle 11\bar{2}0 \rangle$. Each bright dot in the image shows the position of a Ga atomic column. A triangular region was observed at the top edge (the surface-side edge) of the α defect and a pair of defects were observed at the bottom edge (the substrate side edge). The triangle at the top edge was bounded by a (0001) base and $\{11\bar{2}3\}$ sidewalls. The IDBs in heavily Mg-doped GaN are reportedly parallel to (0001) and $\{11\bar{2}3\}$ planes.^{30,31} A pyramidal ID is an example of a closed ID bounded by (0001) and $\{11\bar{2}3\}$ planes.^{17,32,33} We performed a qualitative elemental analysis of the triangular region by EDS in TEM (Fig. 2(b)). The Mg concentrations at the top (0001) base and at the sidewalls (points A and B in the inset) were clearly larger than those measured outside and inside the triangular region (points C and D). In addition, the Mg concentration at the (0001) base (point A) was larger than that at the sidewalls (point B). This Mg distribution agrees with that reported previously at a pyramidal ID.³³ We thus concluded that the triangular region was a closed ID and that the top (0001) base was an IDB with Mg segregation, which was observed in our previous analysis.¹⁴ The present TEM results indicate that the ID is elongated along the $\langle 1\bar{1}00 \rangle$ direction. This is probably because the ID is a part of a dislocation loop that bounds extrinsic $\{11\bar{2}0\}$ planes as described in the following. Along with the growth of the extrinsic defect, the ID would grow along the $\langle 1\bar{1}00 \rangle$ direction to keep the triangular prism shape bounded by (0001) and $\{11\bar{2}3\}$ planes.

The HAADF-STEM image of α defects (Fig. 2(a)) directly shows that two extra (11-20) planes are terminated by the triangular region at the top edge, and a $(11\bar{2}0)$ plane ends at each defect at the bottom edge. The extra lattice planes are easily seen in Fig. 2(c), which shows images of Fig. 2(a) Fourier filtered using $11\bar{2}0$ spots. Thus, these images show that two extra $(11\bar{2}0)$ lattice planes are present between the top and the bottom edges of the α defect, indicating that the Burgers vector of the dislocation that bounds an α defect is $\mathbf{b} = \frac{1}{3}\langle 11\bar{2}0 \rangle$. Furthermore, the HAADF-STEM images of the defects at the bottom edge show that they were closely spaced dislocations along the $\langle 1\bar{1}00 \rangle$ direction and that each dislocation bounds a $(11\bar{2}0)$ lattice plane. This indicates that the defects are partial dislocations with Burgers vectors $\mathbf{b} = \frac{1}{3}\langle 10\bar{1}0 \rangle$, which were generated through dissociation of a perfect dislocation with a Burgers vector $\mathbf{b} = \frac{1}{3}\langle 11\bar{2}0 \rangle$.²⁹ This dissociation reduces the dislocation energy because the dislocation energy is proportional to $|\mathbf{b}|^2$.²⁹ In addition, the STEM image shows that the typical distance between the defects at the bottom edge was 6 nm. This distance, 6 nm, matches the reported distance between basal partial dislocations in GaN in the literature.³⁴ Furthermore, the line connecting the top edge (the triangular region) and the bottom edge (the pair of defects) was about 45° from the [0001] plane, or their slip plane normal. This positional relationship between the top and the bottom edges should be attributed to the Peach-Koehler force between the dislocations at the top edge and those at the bottom edge.²⁹

Defect β , observed as a bright dot in Fig. 1(a), had an extra atomic plane between (0001) planes

of the matrix as described in our previous report (Fig. 2 in Ref¹⁴). The atomic resolution image in the figure directly shows that the Burgers vector of the dislocation bordering the defect was $\mathbf{b} = \frac{1}{2}\langle 0001 \rangle$, and that the dislocation did not dissociate into partial dislocations. The width of the STEM image of defect β along (0001) was 3 to 5 nm in sample C1. Also, γ and δ defects were intrinsic defects on $\{11\bar{2}0\}$ GaN, and their total Burgers vector was $\frac{1}{3}\langle 11\bar{2}0 \rangle$.¹⁴ The diameter of the loops in sample C3 ranged from 50 to 120 nm. In the present study, we have shown that the dislocations at the edges of an α defect with a total Burgers vector of $\mathbf{b} = \frac{1}{3}\langle 11\bar{2}0 \rangle$ dissociate into partial dislocations with a Burgers vector of $\mathbf{b} = \frac{1}{2}\langle 0001 \rangle$. This strongly suggests that the dislocations that bound γ and δ defects should also dissociate into partial dislocations.

Mg atom maps of samples C1 and C3 obtained by APT analyses are shown in Fig. 3, where each green dot corresponds to a Mg atom. In sample C1 (Fig. 3(a)), two types of Mg agglomerations were observed. One was an agglomeration along edges of an oblong along the [1-100] direction (denoted A) and the other was a nano-sized agglomeration (denoted B). Figure 3(b) shows a $(1\bar{1}00)$ cross-section of the Mg distribution in agglomeration A, where the Mg atom distribution in a thin slab across the region of agglomeration A (the shaded slab in Fig. 3(a)) was projected on a $(1\bar{1}00)$ plane. The thickness of the slab was ~ 5 nm. Figures 3(a) and 3(b) show that Mg atoms agglomerate to form a triangular prism region with high Mg concentration at the top edge of the agglomeration. At the bottom edge, Mg atoms agglomerated along a pair of straight lines along the $[1\bar{1}00]$ direction, and Mg atoms were hardly detected on the (0001) plane between the lines. The distance between the lines was about 10 nm. The Mg concentration is quantitatively calculated to be 10 atomic % at the top edge and 0.2 atomic % along each line at the bottom edge. The Mg concentration in the matrix is 0.02 atomic %. The shape and the crystallographic orientation of the top and the bottom edges of agglomeration A indicate that Mg atoms agglomerated at the dislocation that bounds α defect.

The nano-sized Mg agglomerations in sample C1 (Fig. 3 (a)) appear as a flat-disk or a flat-doughnut on the (0001) plane. Figure 3(c) shows closeup views of the flat-doughnut shaped agglomeration (agglomeration B in Fig. 3(a)), as an example. The left and the right panes in the figure show the agglomeration B viewed in the $\langle 11\bar{2}0 \rangle$ and $\langle 0001 \rangle$ directions, respectively. The inner diameter of the doughnuts was about 5 nm. The average Mg concentration in the nano-sized agglomeration is 1 atomic %. In sample C3 (Fig. 3(d)), Mg agglomerations on loop edges are observed (denoted C), while nano-sized Mg agglomerations are not observed in this APT data. Figure 3(e) shows a closeup image of the loop-like agglomeration C. The loop-like agglomeration lies on $\{11\bar{2}0\}$, and its diameter was about 80 nm. The Mg concentration at the loop edge was 0.2 atomic %. The above APT results indicate that the agglomerations denoted B and C should represent Mg distribution at the edges of β and γ defects in Fig. 1, respectively, because the shape, size, and crystallographic orientation of the agglomerations agree with those of the respective defects. The TEM and APT results are summarized in Table II.

Figure 3 shows 3D Mg atom maps obtained by APT analyses in samples C1 and C3. Each green dot in the figure shows a Mg atomic position. In sample C1 (Fig. 3(a)), two types of Mg agglomerations were observed. One was agglomerated along edges of oblongs (denoted A) and the other was nano sized Mg agglomerations (denoted B). Figure 3 (b) shows a $(1\bar{1}00)$ cross-section of the Mg agglomeration A. At the top edge of the agglomeration A, the Mg concentration was ~ 10 atomic % and the form was a triangular prism. At the bottom edge, Mg atoms agglomerated along a pair of straight line along $\langle 1\bar{1}00 \rangle$, and the distance between the lines was about 10 nm. The Mg concentration along each line was 0.2 atomic %. Figure 3(c) shows closeup images of the nano-sized agglomeration B viewed in the $\langle 11\bar{2}0 \rangle$ and $\langle 0001 \rangle$ directions. The nano-size Mg agglomeration appeared as a flat-disk or a flat-doughnut on a (0001) plane. The average Mg concentration at defects on the (0001) plane was about 1 atomic %. The inner diameter of the doughnuts was about 5 nm. In sample C3 (Fig. 3(d)), Mg agglomerations were observed on loop edges (denoted C), but nano-sized Mg agglomerations B were not. Fig. 3(e) is a closeup image of the loop-like agglomeration C, which shows that the loop lies on the $\{11\bar{2}0\}$ plane. The Mg concentration at the loop edge was 0.2 atomic %. The diameter of the loop was about 80 nm.

The complementary TEM and APT results have revealed that Mg atoms agglomerate at dislocations that bound extended defects. This indicates that the observed agglomeration is caused by the effective pressure of the dislocations, *i.e.*, Cottrell atmosphere.^{29,35-37} Impurity (Mg) atoms would agglomerate at a dislocation to reduce the pressure and the energy of the dislocation, and the impurity concentration in the Cottrell atmosphere would increase with the pressure around the dislocation.^{29,38} For an edge dislocation with Burgers vector \mathbf{b} , the effective pressure around the dislocation is proportional to $|\mathbf{b}|$.²⁹ Our results show that the Mg concentration at a β defect (1 atomic %) is larger than those at a γ defect and at the bottom edge of an α defect (0.2 atomic %), and the magnitudes of the Burgers vectors of β defects are larger than those of Burgers vectors of α and γ defects. We did not find agglomeration at δ defects in the present analysis. This could be attributed to the small amount of Mg atoms at those defects because the defects are very small (a few nanometers in diameter) and the magnitudes of their Burgers vectors are small. We cannot exclude the possibility that the defect was not included in the volume analyzed in the present analysis.

B. CL and PAS results

Figure 4(a) shows CL spectra for the samples C1, C2, and C3. The spectra show that the intensity of DAP emission around 3.28 eV increases with the annealing temperature. Furthermore, the intensity of GL around 2.35 eV, which originates from V_N -related defects,²¹ decreased when the annealing temperature was increased. These results indicate that annealing at an elevated temperatures increases Mg acceptor concentration and decreases the concentrations of V_N -related defects and non-radiative recombination centers.²¹

To quantitatively examine the isochronal and the isothermal changes in the CL spectra, we plotted integrated intensities of DAP and of GL against the annealing temperature (Fig. 4(b)) and against annealing duration (Fig. 4(c)). The solid and open circles in the figures show the integrated DAP intensities and the integrated GL intensities, respectively. Figure 4(b) shows that the integrated DAP intensity clearly increased from sample C1 to sample C2, whereas the difference in the DAP intensities between samples C2 and C3 was small. The integrated GL intensity clearly decreased from sample C1 to sample C2, whereas the difference in the GL intensity between sample C2 and C3 was small. Similarly, in Fig. 4(c), the integrated DAP intensities of samples T2 to T5 were clearly larger than those of samples C1 and T1, whereas the differences in the DAP intensities of samples T2 to T5 were small. The integrated GL intensity clearly decreased from sample C1 to T1, whereas the differences in the GL intensities of the samples T1 to T5 were small. Therefore, the DAP intensities indicate that the Mg acceptor activation ratio increases with increasing annealing temperature in the early stage of the isochronal annealing (1573 to 1673 K) and increases with increasing duration in the isothermal annealing (0 to 30 min). Furthermore, the GL intensities indicate that the concentration of the compensating centers decreases with increasing annealing temperature (duration) in the early stage of the isochronal (isothermal) annealing. In the later stages of the isochronal and the isothermal annealing, no clear changes were observed in the acceptor activation ratio or the concentration of the compensating centers. These results are consistent with those of the recent investigations of Mg activation ratios using Hall-effect measurement.^{13,39} The TEM results (Fig. 1) indicate that the α and β defects were observed in samples C1 and T1, but not in samples C2, C3, and T2 to T5. This strongly suggests that the lower activation ratios in samples C1 and T1 are attributed to the α and β defects.

Figures 5(a) and 5(b) show the isochronal and isothermal changes in values of S parameters, respectively. In the isochronal annealing (Fig. 5(a)), the S values measured without the laser illumination (denoted Dark in the diagram) were almost the same. The diagram also shows that the laser illumination (denoted Illuminated in the diagram) increased the S values. The S value of sample C1 under the laser illumination was larger than the S values of the other samples, whereas the S values of the other samples under the laser illumination were nearly the same within experimental errors. In the isothermal annealing (Fig. 5(b)), the S values measured without the laser illumination were almost the same within the experimental error, except that for T0, which was larger than those for the other samples. The S values of samples C1 and T0 under the laser illumination were clearly larger than those of the other samples.

The S value of sample T0 without the laser illumination (Fig. 5(b)) indicates that the probability of positron trapping by negatively charged vacancy-type defects is larger in sample T0 than those in the other samples. That means such vacancies are eliminated at the very initial stage of the present annealing. The difference in the S values in Fig. 5 measured with and without the laser illumination shows that the concentrations of positively charged defects (V_+) and neutral defects (V_0)

in samples T0 and C1 are significantly larger than those in the other samples. Since a V_N in GaN is positively charged,⁴⁰ the S values in the samples T0 and C1 indicate that the amount of vacancy clusters such as $(V_{Ga})_m(V_N)_n$ [n, m : integer] in those samples is larger than those in the other samples.

The isochronal and isothermal changes in the values of S parameter measured with the laser illumination (Fig. 5) agree well with the isochronal and isothermal changes in the GL intensities (Figs. 4(b) and 4(c)), which indicates that some of the $(V_{Ga})_m(V_N)_n$ -type vacancies detected in the PAS measurement should be responsible for the GL. In addition, the analysis of the S parameters and the analysis of GL intensities indicate that the concentrations of the vacancy-type defects in samples C2, C3, and T2 to T5 are lower than those in samples C1 and T1. This result is consistent with the TEM results (Figs. 1) that observed intrinsic-type extended defects in samples C2, C3, and T2 to T5. This is because intrinsic-type extended defects are produced by agglomeration of vacancies, which should decrease the concentration of vacancies.

IV. Discussion

We previously showed that no extended defects were found in Mg-ion-implanted samples before annealing.¹⁴ This indicates that the Mg ion implantation produced point defects (vacancies and interstitials) and their complexes that could not be observed in the TEM analysis. The present TEM observations have clarified that, in both isochronal and isothermal annealing, extrinsic defects (denoted α and β) form in the early stage of the annealing, while intrinsic defects (denoted γ and δ) form in the later stage of the annealing. Intrinsic extended defects are formed by agglomeration of vacancies, and extrinsic extended defects are formed by agglomeration of interstitials. The change in the nature of the defects between the annealing stages, i.e., from the extrinsic defects to the intrinsic defects, can be explained by the difference between the migration energies of the point defects in GaN. This is because the migration energies of V_N and V_{Ga} are reportedly larger than those of N_i and Ga_i when the Fermi level is high in the band gap.^{40,41} The diffusion or migration of the point defects, which determines the structure and size of extended defects, is a thermally activated process, which can be described by Arrhenius expressions.⁴²⁻⁴⁴ Therefore, we conclude that the evolution of the extended defects is driven by such thermally activated diffusion of point defects.

The present TEM analysis in combination with CL and PAS analyses clarified that Mg acceptor formation well correlates with the elimination of the extended defects with highly Mg-rich regions (α and β defects). We previously reported the SIMS analysis of Mg and Mg acceptor distribution in a sample prepared using the same conditions as for sample C1. (Ref⁴⁵, Fig. 1(b)). The result indicated that the Mg acceptor concentration decreased in the depth range 200 to 500 nm from the sample surface, where α and β defects were observed in the present analysis. The results also indicated that a clear increase in Mg concentration provides a peak at the depth of 350 nm. The present APT analysis indicates that the increase in the Mg concentration would mainly be due to the Mg

agglomeration at IDBs of α defects because the Mg concentration at the IDBs is 500 times larger than that of the matrix and 10 times larger than that at β defects. Thus, the observed decrease in the Mg acceptor concentration in the depth range of 200 nm to 500 nm strongly suggests that β defects would also reduce the Mg acceptor formation. We have shown that the Mg concentration in the Cottrell atmosphere around β defects significantly exceeds the solubility limit of Mg (0.2 atomic % or less).^{46,47} This strongly suggest that Mg nitride forms around β defects.⁴⁸ Forming Mg-nitride-like structures should reduce the Mg acceptor formation in samples C1 and T1.⁴⁸ Such structure could form at the dislocation core that bounds a β defect because non-stoichiometric core structures are often found experimentally in compound semiconductors, including GaN.⁴⁹⁻⁵² Further structural analysis of the dislocation is now in progress.

V. Summary

Using TEM, APT, CL and PAS, we analyzed crystallographic features of extended defects and Mg agglomeration in Mg-ion-implanted GaN after annealing, and investigated their impacts on Mg acceptor activation.

The following conclusions were obtained:

1. The extrinsic defects (denoted α and β) form and disappear in the early stages of the annealing, and intrinsic defects (denoted γ and δ) form in the later stages. We determined the Burgers vector of the dislocation that bound β defects to be $\frac{1}{2}\langle 0001 \rangle$, while that of the dislocations bounding the other defects is $\frac{1}{3}\langle 11\bar{2}0 \rangle$. The latter should split into partial dislocations with $\mathbf{b}=\frac{1}{3}\langle 10\bar{1}0 \rangle$. The top edge of an α defect consists of a thin triangular-shaped inversion domain.
2. Mg concentration at the edge of β defects is 1 atomic % and that at the edges of the other defects is 0.2 atomic %. The significantly larger Mg concentration at the edge of β defects is attributed to the large magnitude of $|\mathbf{b}|^2$ for Cottrell atmosphere. Mg agglomeration at IDBs of α defects inactivates Mg atoms. Mg agglomeration at β defects could reduce Mg acceptor formation since the Mg concentration at the defect exceeds the solubility limit of Mg in GaN, forming Mg-nitride-like structure.
3. The DAP intensities, which represent the formation of Mg acceptor, increases in the early stage of the annealing, *i.e.*, while α and β defects form and disappear, then they saturate in the later stage. On the other hand, the GL intensities, which represent the concentration of V_N -related defects, significantly decreases in the early stage of the annealing. In the PAS analysis, S parameter, which represents the concentration of vacancy-type defects, indicates that the vacancy-type defects are eliminated in the early stage of the annealing. Furthermore, S parameter measured under He-Cd laser illumination indicate that the concentration of V_N -related vacancy clusters such as $(V_{Ga})_m(V_N)_n$ [n, m : integer] decreases at the very initial stage of the annealing.

Based on the above results, we conclude that, in the early stage of the post-implantation annealing, the extrinsic defects and Mg agglomeration at the defects, as well as the compensating centers such as V_N -related defects, would inhibit the formation of *p*-type GaN. These defects can be eliminated by elevating the annealing temperature or by prolonging the annealing duration, which enables the formation of *p*-type GaN.

Acknowledgement

The authors would like to thank professor Atsushi Oshiyama and Professor Kenji Shiraishi for their valuable discussions on electronic structures of defects in Mg-doped GaN. Part of this work was supported by the MEXT "Program for research and development of next-generation semiconductor to realize energy-saving society" (JPJ005357), the MEXT "Program for Creation of Innovative Core Technology for Power Electronics" (JPJ009777), JSPS KAKENHI (JP16H06424 and 21H01826), and by Nagoya University microstructural characterization platform as a program of MEXT "Nanotechnology Platform". A part of this research was also supported by the Polish National Science Centre through project No 2018/29/B/ST5/00338 as well as by the Polish National Centre for Research and Development through project TECHMATSTRATEG-III/0003/2019-00.

Reference

- ¹ S. Chowdhury, *Phys. Status Solidi Appl. Mater. Sci.* **212**, 1066 (2015).
- ² I.C. Kizilyalli, A.P. Edwards, O. Aktas, T. Prunty, and D. Bour, *IEEE Trans. Electron Devices* **62**, 414 (2015).
- ³ B.N. Feigelson, T.J. Anderson, M. Abraham, J.A. Freitas, J.K. Hite, C.R. Eddy, and F.J. Kub, *J. Cryst. Growth* **350**, 21 (2012).
- ⁴ T. Oikawa, Y. Saijo, S. Kato, T. Mishima, and T. Nakamura, *Nucl. Inst. Methods Phys. Res. B* **365**, 168 (2015).
- ⁵ T.J. Anderson, J.D. Greenlee, B.N. Feigelson, J.K. Hite, F.J. Kub, and K.D. Hobart, *ECS J. Solid State Sci. Technol.* **5**, Q176 (2016).
- ⁶ T. Niwa, T. Fujii, and T. Oka, *Appl. Phys. Express* **10**, 091002 (2017).
- ⁷ R. Tanaka, S. Takashima, K. Ueno, H. Matsuyama, M. Edo, and K. Nakagawa, *Appl. Phys. Express* **12**, 054001 (2019).
- ⁸ H. Sakurai, M. Omori, S. Yamada, Y. Furukawa, H. Suzuki, T. Narita, K. Kataoka, M. Horita, M. Bockowski, J. Suda, and T. Kachi, *Appl. Phys. Lett.* **115**, 142104 (2019).
- ⁹ K. Kataoka, T. Narita, H. Iguchi, T. Uesugi, and T. Kachi, *Phys. Status Solidi* **255**, 1700379 (2018).
- ¹⁰ K. Shima, H. Iguchi, T. Narita, K. Kataoka, K. Kojima, A. Uedono, and S.F. Chichibu, *Appl. Phys. Lett.* **113**, 191901 (2018).
- ¹¹ T. Narita, H. Yoshida, K. Tomita, K. Kataoka, H. Sakurai, M. Horita, M. Bockowski, N. Ikarashi, J. Suda, T. Kachi, and Y. Tokuda, *J. Appl. Phys.* **128**, 090901 (2020).
- ¹² M. Horita, S. Takashima, R. Tanaka, H. Matsuyama, K. Ueno, M. Edo, T. Takahashi, M. Shimizu, and J. Suda, *Jpn. J. Appl. Phys.* **56**, 031001 (2017).
- ¹³ K. Hirukawa, K. Sumida, H. Sakurai, H. Fujikura, M. Horita, Y. Otoki, K. Sierakowski, M. Bockowski, T. Kachi, and J. Suda, *Appl. Phys. Express* **14**, 056501 (2021).
- ¹⁴ K. Iwata, H. Sakurai, S. Arai, T. Nakashima, T. Narita, K. Kataoka, M. Bockowski, M. Nagao, J. Suda, T. Kachi, and N. Ikarashi, *J. Appl. Phys.* **127**, 105106 (2020).
- ¹⁵ T. Nakashima, E. Kano, K. Kataoka, S. Arai, H. Sakurai, T. Narita, K. Sierakowski, M. Bockowski, M. Nagao, J. Suda, T. Kachi, and N. Ikarashi, *Appl. Phys. Express* **14**, 011005 (2021).
- ¹⁶ A. Kumar, J. Uzuhashi, T. Ohkubo, R. Tanaka, S. Takashima, M. Edo, and K. Hono, *J. Appl. Phys.* **126**, (2019).
- ¹⁷ K. Iwata, T. Narita, M. Nagao, K. Tomita, K. Kataoka, T. Kachi, and N. Ikarashi, *Appl. Phys. Express* **12**, 031004 (2019).
- ¹⁸ B. Monemar, P.P. Paskov, G. Pozina, C. Hemmingsson, J.P. Bergman, T. Kawashima, H. Amano, I. Akasaki, T. Paskova, S. Figge, D. Hommel, and A. Usui, *Phys. Rev. Lett.* **102**, 235501 (2009).
- ¹⁹ G. Pozina, P.P. Paskov, J.P. Bergman, C. Hemmingsson, L. Hultman, B. Monemar, H. Amano, I.

- Akasaki, and A. Usui, *Appl. Phys. Lett.* **91**, 221901 (2007).
- ²⁰ M.A. Reshchikov, D.O. Demchenko, J.D. McNamara, S. Fernández-Garrido, and R. Calarco, *Phys. Rev. B* **90**, 035207 (2014).
- ²¹ K. Kojima, S. Takashima, M. Edo, K. Ueno, M. Shimizu, T. Takahashi, S. Ishibashi, A. Uedono, and S.F. Chichibu, *Appl. Phys. Express* **10**, 061002 (2017).
- ²² A. Uedono, H. Iguchi, T. Narita, K. Kataoka, W. Egger, T. Koschine, C. Hugenschmidt, M. Dickmann, K. Shima, K. Kojima, S.F. Chichibu, and S. Ishibashi, *Phys. Status Solidi Basic Res.* **256**, 1 (2019).
- ²³ A. Uedono, H. Sakurai, T. Narita, K. Sierakowski, M. Bockowski, J. Suda, S. Ishibashi, S.F. Chichibu, and T. Kachi, *Sci. Rep.* **10**, 17349 (2020).
- ²⁴ A. Kumar, W. Yi, J. Uzuhashi, T. Ohkubo, J. Chen, T. Sekiguchi, R. Tanaka, S. Takashima, M. Edo, and K. Hono, *J. Appl. Phys.* **128**, 065701 (2020).
- ²⁵ Q. Yan, A. Janotti, M. Scheffler, and C.G. Van de Walle, *Appl. Phys. Lett.* **100**, 142110 (2012).
- ²⁶ F. Tuomisto and I. Makkonen, *Rev. Mod. Phys.* **85**, 1583 (2013).
- ²⁷ A. Uedono, S. Takashima, M. Edo, K. Ueno, H. Matsuyama, W. Egger, T. Koschine, C. Hugenschmidt, M. Dickmann, K. Kojima, S.F. Chichibu, and S. Ishibashi, *Phys. Status Solidi Basic Res.* **255**, 1700521 (2018).
- ²⁸ H. Iguchi, T. Narita, K. Kataoka, M. Kanechika, and A. Uedono, *J. Appl. Phys.* **126**, 125102 (2019).
- ²⁹ D. Hull and D.J. Bacon, *Introduction to Dislocations* (Butterworth-Heinemann, Oxford, 2011).
- ³⁰ L.T. Romano, J.E. Northrup, A.J. Ptak, and T.H. Myers, *Appl. Phys. Lett.* **77**, 2479 (2000).
- ³¹ S. Pezzagna, P. Vennéguès, N. Grandjean, and J. Massies, *J. Cryst. Growth* **269**, 249 (2004).
- ³² Z. Liliental-Weber, M. Benamara, W. Swider, J. Washburn, I. Grzegory, S. Porowski, D.J.H. Lambert, C.J. Eiting, and R.D. Dupuis, *Appl. Phys. Lett.* **75**, 4159 (1999).
- ³³ P. Vennéguès, M. Leroux, S. Dalmasso, M. Benaissa, P. De Mierry, P. Lorenzini, B. Damilano, B. Beaumont, J. Massies, and P. Gibart, *Phys. Rev. B* **68**, 235214 (2003).
- ³⁴ K. Suzuki and S. Takeuchi, *Philos. Mag. Lett.* **79**, 423 (1999).
- ³⁵ P.B. Hirsch, *J. Microsc.* **118**, 3 (1980).
- ³⁶ K. Thompson, P.L. Flaitz, P. Ronsheim, D.J. Larson, and T.F. Kelly, *Science* (80-.). **317**, 1370 (2007).
- ³⁷ S. Duguay, T. Philippe, F. Cristiano, and D. Blavette, *Appl. Phys. Lett.* **97**, 13 (2010).
- ³⁸ D. McLean, *Grain Boundaries in Metals* (Clarendon Press, London, 1957).
- ³⁹ K. Sumida, K. Hirukawa, H. Sakurai, K. Sierakowski, M. Horita, M. Bockowski, T. Kachi, and J. Suda, *Appl. Phys. Express* **14**, 121004 (2021).
- ⁴⁰ S. Limpijumngong and C. Van de Walle, *Phys. Rev. B* **69**, 035207 (2004).
- ⁴¹ A. Kyrtos, M. Matsubara, and E. Bellotti, *Phys. Rev. B* **93**, 245201 (2016).
- ⁴² P.M. Fahey, P.B. Griffin, and J.D. Plummer, *Rev. Mod. Phys.* **61**, 289 (1989).
- ⁴³ C. Bonafos, D. Mathiot, and A. Claverie, *J. Appl. Phys.* **83**, 3008 (1998).
- ⁴⁴ R.E. Smallman and A.H.W. Ngan, *Modern Physical Metallurgy: Eighth Edition* (Elsevier, 2013).

- ⁴⁵ H. Sakurai, T. Narita, M. Omori, S. Yamada, A. Koura, M. Iwinska, K. Kataoka, M. Horita, N. Ikarashi, M. Bockowski, J. Suda, and T. Kachi, *Appl. Phys. Express* **13**, 086501 (2020).
- ⁴⁶ D.P. Bour, H.F. Chung, W. Götz, L. Romano, B.S. Krusor, D. Hofstetter, S. Rudaz, C.P. Kuo, F.A. Ponce, N.M. Johnson, M.G. Craford, and R.D. Bringans, *MRS Proc.* **449**, 509 (1996).
- ⁴⁷ G. Namkoong, E. Trybus, K.K. Lee, M. Moseley, W.A. Doolittle, and D.C. Look, *Appl. Phys. Lett.* **93**, 1 (2008).
- ⁴⁸ C.G. Van De Walle, C. Stampfl, and J. Neugebauer, *J. Cryst. Growth* **189–190**, 505 (1998).
- ⁴⁹ Y. Xin, E.M. James, I. Arslan, S. Sivananthan, N.D. Browning, S.J. Pennycook, F. Omnès, B. Beaumont, J.P. Faurie, and P. Gibart, *Appl. Phys. Lett.* **76**, 466 (2000).
- ⁵⁰ S. Lopatin, S.J. Pennycook, J. Narayan, and G. Duscher, *Appl. Phys. Lett.* **81**, 2728 (2002).
- ⁵¹ I. Belabbas, P. Ruterana, J. Chen, and G. Nouet, *Philos. Mag.* **86**, 2241 (2006).
- ⁵² K. Tillmann, L. Houben, and A. Thust, *Philos. Mag.* **86**, 4589 (2006).

Tables

Table I Annealing conditions.

Sample	Temp. (K)	Duration (min)
C1	1573	
C2	1673	5
C3	1753	
T0		0.5
T1		15
T2		30
T3	1573	60
T4		90
T5		120

Table II STEM results (ADF-STEM image and Burgers vectors) and APT results (Mg concentrations at dislocations).

Defect	ADF image	Defect nature	Burgers vector	Mg concentration (at. %)	Mg agglomeration
α	Oblong	$\{11\bar{2}0\}$ extrinsic	$\frac{1}{3}\langle 10\bar{1}0 \rangle$	0.2 (10 at the top edge)	A
β	Dot	(0001) extrinsic	$\frac{1}{2}\langle 0001 \rangle$	1.0	B
γ	Loop	$\{11\bar{2}0\}$ intrinsic	$\frac{1}{3}\langle 10\bar{1}0 \rangle$	0.2	C
δ	Dot	$\{11\bar{2}0\}$ intrinsic	$\frac{1}{3}\langle 10\bar{1}0 \rangle$	Not detected	Not detected

Figure captions

Figure 1. ADF-STEM cross-sectional images of the samples. Isochronal evolution of the defects is seen in (a), (b), and (c). Isothermal evolution of the defects is seen in (a), (d), (e), and (f). Scale bars are 200 nm. In the early stage of the annealing ((a) and (d)), defects are observed as bright oblongs (α) and dots (β). In the later stage of the annealing ((b), (c), (e) and (f)), defects are observed as bright loops (γ) and dots (δ). α and β defects were distributed in the depth range 200 to 500 nm from the sample surface.

Figure 2. (a) A HAADF-STEM image of α defect (oblong defect) viewed in the $\langle 1\bar{1}00 \rangle$ direction. A triangular-shaped defect was observed at the top edge, while two defects were observed at the bottom edge. The triangle was bounded by a (0001) base and $\{11\bar{2}3\}$ sidewalls. (b) EDS results on the triangular-shaped defect. Mg concentration clearly increases at the (0001) boundary and at the side wall. (c) Fourier filtered images of defects in (a) using $11\bar{2}0$ spots. Two additional $(11\bar{2}0)$ lattice planes are observed between the top and the bottom edges of the defect.

Figure 3. 3D Mg atom maps obtained by APT technique in samples (a–c) C1 and (d–e) C3. In sample C1, two types of Mg agglomeration were observed: Mg agglomeration along edges of oblongs (denoted A) and nano-sized Mg agglomerations (denoted B). (b) $(1\bar{1}00)$ cross section of the agglomeration A. Triangular-shaped Mg agglomeration was seen at the top edge. Open triangles at the bottom edge indicate Mg agglomeration along a pair of straight lines along $\langle 1\bar{1}00 \rangle$. (c) Closeup images of the agglomeration B. left (right) panel shows Mg agglomeration viewed in the $\langle 11\bar{2}0 \rangle$ ($\langle 0001 \rangle$) direction. The atom map shows a flat doughnut-shaped agglomeration. (d) Agglomeration along a loop edge was seen in sample C3 (denoted C). (e) Closeup image of the agglomeration C.

Figure 4. (a) Isochronal changes in CL spectra. Integrated intensities of DAP and GL during (b) isochronal annealing and (c) isothermal annealing. Close and open circles show integrated DAP intensity (left axis) and integrated GL intensity (right axis), respectively.

Figure 5. (a) isochronal and (b) isothermal changes in S parameters in PAS analysis. The S values measured without and with the laser illumination are denoted Dark and Illuminated in the diagram, respectively.

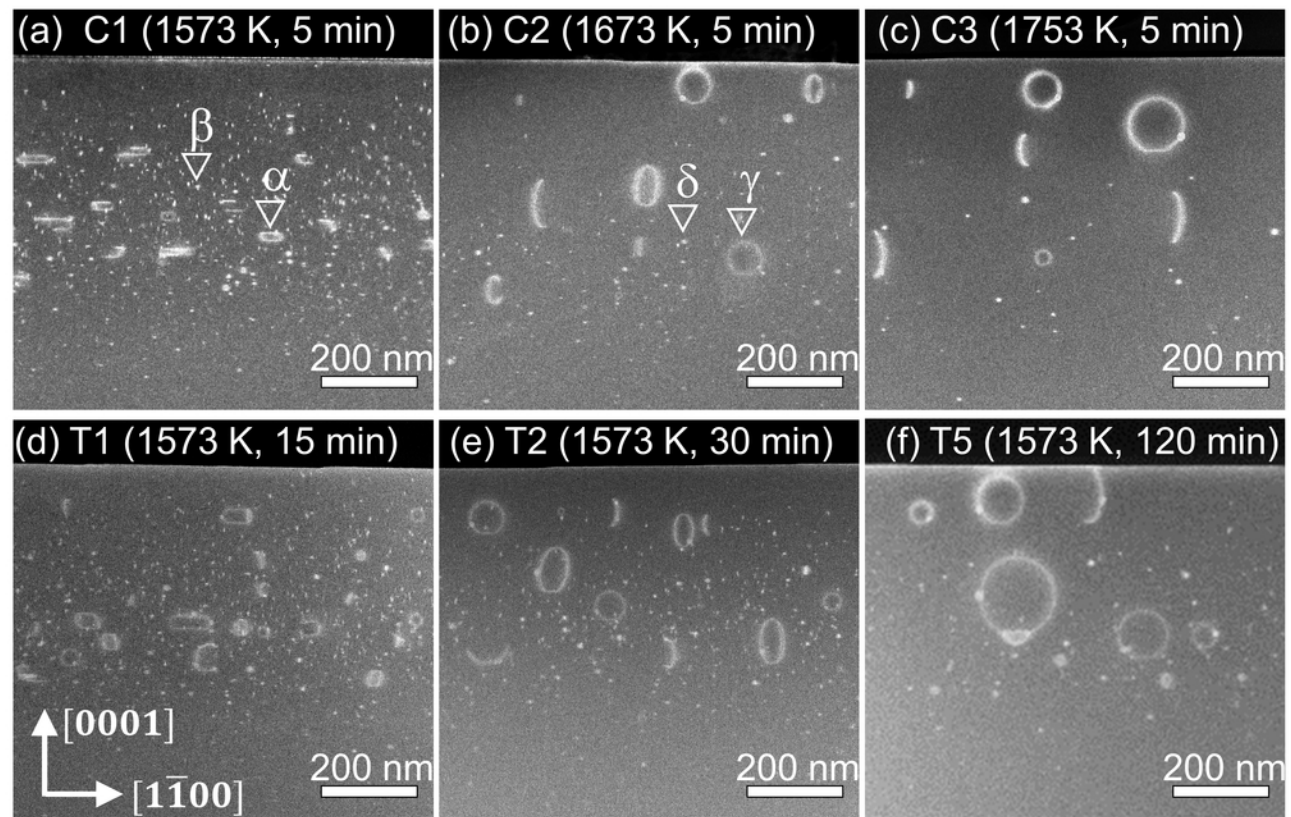


Figure 1

double

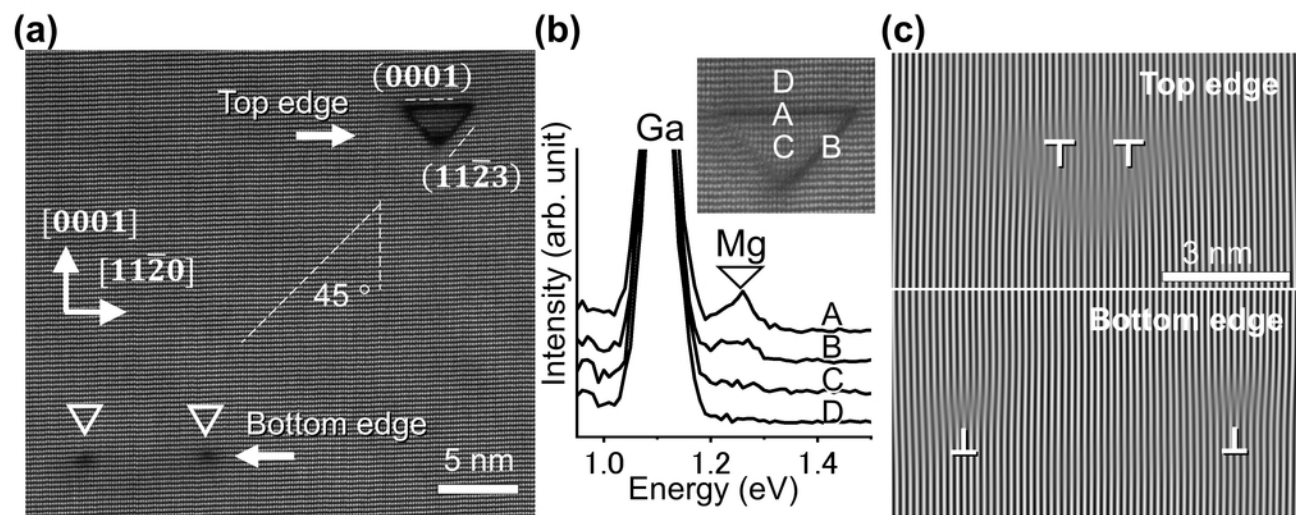


Figure 2

double

(a) C1 (1573 K, 5 min) (b) Agglomeration A (d) C3 (1753 K, 5 min) (e) Agglomeration C

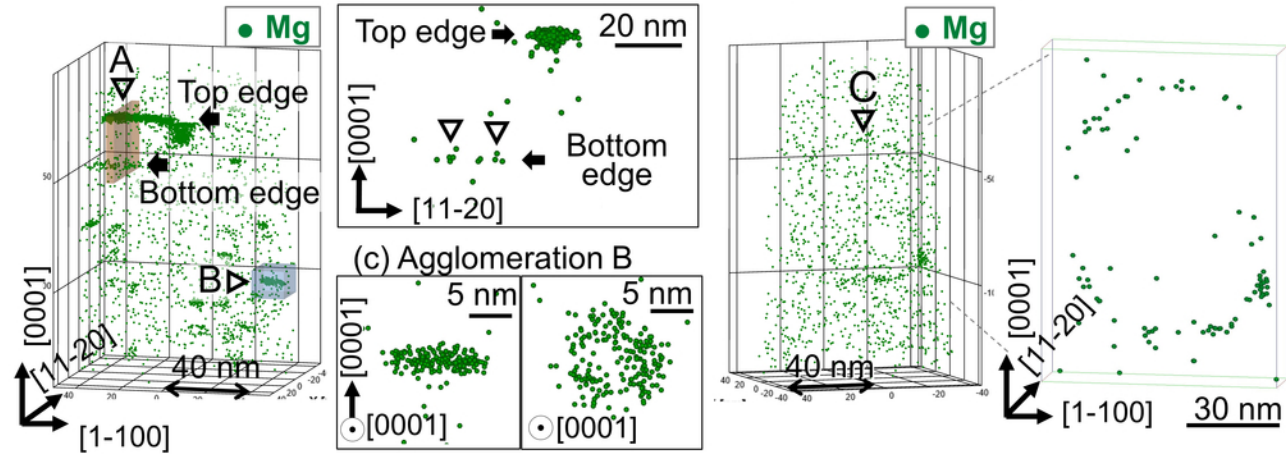


Figure 3

double

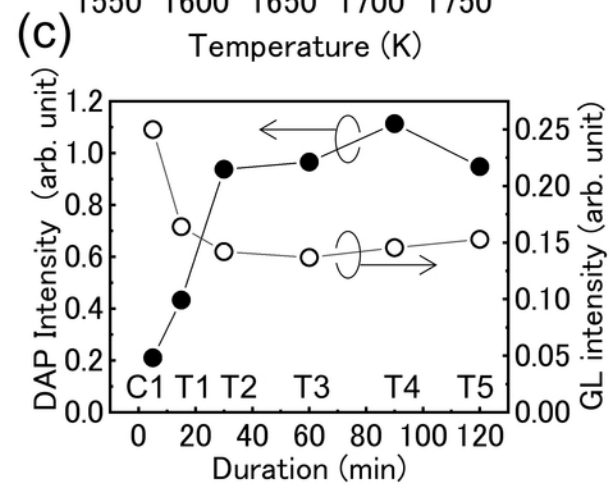
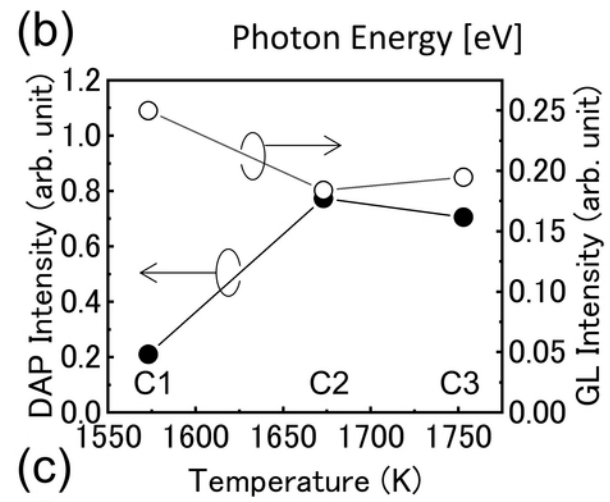
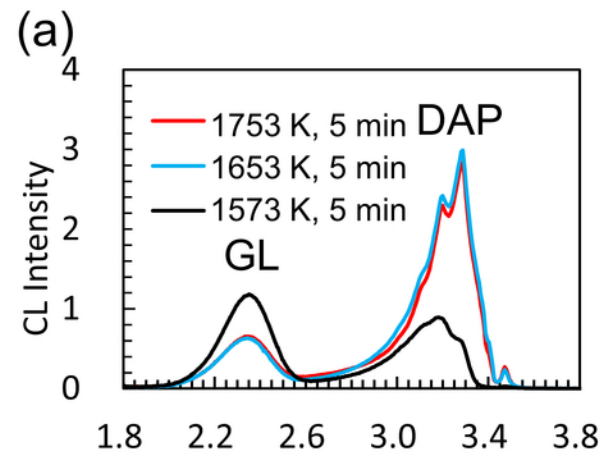


Figure 3

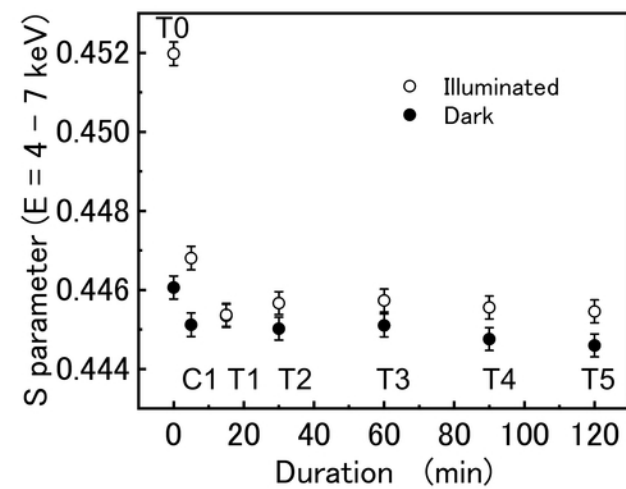
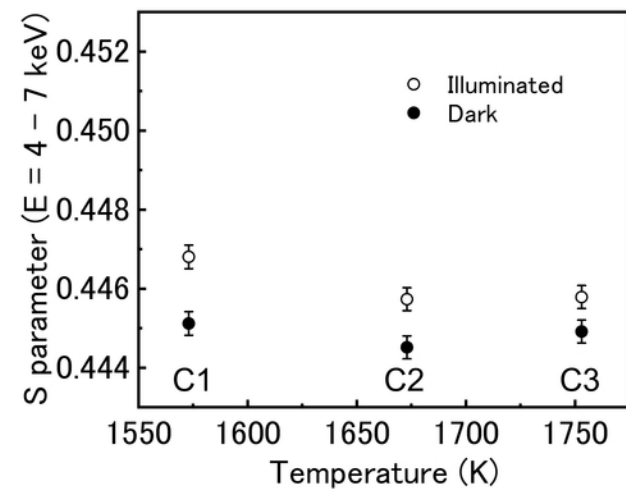


Figure 5

single